Article | Received 14 September 2026; Revised 21 October 2026; Accepted 2 November 2026; Published 13 November 2026
https://doi.org/10.55092/aimat20260014

Unraveling the activity origin of M_2CO_2 MXene-supported single-atom catalysts for nitrate electroreduction: a combined DFT and machine learning study

Jing Xu[1,*], Yuqi Qiu[1], Wenxi Han[1], Jinghao Zhang[1], Yuan Li[1], Xueru Wang[1], Jifa Fu[1], Wenxuan An[1], Zhanchi Zhao[1], Xiaojie Liu[1], Guang Zhao[2], Yong Liu[3] and Lianming Zhao[1,*]

[1] Shandong Key Laboratory of Intelligent Energy Materials, School of Materials Science and Engineering, China University of Petroleum (East China), Qingdao, China
[2] School of Petroleum Engineering, China University of Petroleum (East China), Qingdao, China
[3] Department of Chemistry, University of Colorado Denver, Denver, USA

* Correspondence authors; E-mails: xujing@upc.edu.cn (J.X.); lmzhao@upc.edu.cn (L.Z.).

Highlights:

- DFT screened 150 TM@M_2CO_2 MXene catalysts for NO_3RR.
- CuI@Mo_2CO_2 and RuII@W_2CO_2 show ultra-low U_L of −0.38 and −0.45 V, respectively.
- Machine learning identifies $L_{TM\text{-}O}$, ΔG_{*NO_3}, and χ_p as influential descriptors.
- SHAP reveals nonlinear associations between structural descriptors and limiting potential.

Abstract: Electrocatalytic nitrate reduction to ammonia (NO_3RR) offers a transformative route for pollutant remediation and green synthesis, yet rational catalyst design remains challenging. We combined density functional theory (DFT) with machine learning (ML) to study TM@M_2CO_2 systems (M = Mo, W, and Cr; TM = 3d–5d metals). Of the 150 models, 16 passed screening for stability (formation energy and dissolution potential) and selectivity (suppression of the hydrogen evolution reaction, HER). Their limiting potentials (U_L) were −0.38 V for CuI@Mo_2CO_2 and −0.45 V for RuII@W_2CO_2. These two systems are the most promising NO_3RR candidates among the systems studied. Mechanistic and kinetic analyses confirmed that both catalysts can activate nitrate effectively and exhibit lower barriers for the potential-determining step than for HER. Feature-importance and Shapley Additive Explanations (SHAP) analyses identified the average TM–O bond length ($L_{TM–O}$), nitrate adsorption free energy (ΔG_{*NO_3}), and TM electronegativity (χ_P) as influential descriptors, revealing a nonmonotonic association between ($L_{TM–O}$) and the predicted limiting potential. This work identifies two theoretically promising catalyst candidates and quantifies descriptor importance, offering a data-driven framework for the rational design of MXene-based single-atom catalysts.

Keywords: nitrate reduction reaction; MXene; first-principles calculations; machine learning

Copyright©2026 by the authors. Published by ELSP. This work is licensed under Creative Commons Attribution 4.0 International License, which permits unrestricted use, distribution, and reproduction in any medium provided the original work is properly cited.

1. Introduction

Nitrate pollution has emerged as a major challenge in water environmental remediation and sustainable nitrogen cycling [1]. Continuous inputs from industrial emissions, agricultural fertilization, and domestic wastewater have led to a persistent increase in nitrate concentrations in water bodies. Although conventional nitrogen removal technologies, such as reverse osmosis, ion exchange, and biological denitrification, have been widely applied, they generally suffer from high energy consumption, stringent operational conditions, and complex post-treatment processes [2,3]. Therefore, developing novel nitrate conversion strategies that simultaneously achieve pollution control and resource recovery has attracted growing interest as a promising approach for sustainable nitrogen management [3,4].

The electrocatalytic nitrate reduction reaction (NO_3RR) can overcome these limitations by removing pollutants and recovering resources under mild conditions [4]. Unlike conventional "removal-based" processes, NO_3RR utilizes electrons to convert nitrate into high-value products such as ammonia [4,5]. Ammonia is not only an essential agricultural fertilizer and fundamental chemical feedstock but also a promising hydrogen storage medium and energy carrier. Therefore, green and efficient electrocatalytic ammonia synthesis holds significant application potential [5,6].

NO_3RR is a complex multi-electron, multi-proton process. Nitrate is converted stepwise via NO_3^-, NO_2^-, NO, and NH_2OH, and several competing pathways form the reaction network [3–5]. The hydrogen evolution reaction (HER) competition, nitrite accumulation, and poorly matched intermediate adsorption energies lower Faradaic efficiency and ammonia yield [6,7]. An effective catalyst must bind and activate nitrate with moderate strength while steering later hydrogenation steps away from side reactions [8,9].

Carbon-, metal-, and composite-based catalysts have been explored for NO_3RR [7,8]. Cu-based catalysts remain of interest due to their moderate binding of nitrogen-containing intermediates and partial suppression of HER [9]. Conventional catalysts, however, often have poorly defined active sites and low atom utilization. Single-atom catalysts (SACs) offer maximum atomic utilization, well-defined active sites, and tunable local electronic environments, and have therefore moved NO_3RR catalyst development from empirical screening toward rational design [10,11]. SAC performance depends on the metal center, the coordination environment, and electronic coupling between the support and the active site [12]. MXenes are attractive supports because of their metallic conductivity, abundant surface terminations, and two-dimensional (2D) confinement [13,14]. These transition-metal carbides/nitrides stabilize anchored single atoms and tune the electronic structure of the active centers through surface terminations and interfacial effects [15,16], making them useful platforms for active-site modulation in electrocatalysis [16,17].

Experimental work on MXene-based NO_3RR catalysts is still at an early stage [17,18]. An Ag/Cu–MXene tandem structure improved stepwise nitrate reduction [19]. A 2D MnO_2/MXene heterostructure showed fast charge transfer [20], and a Ru/Cu@MXene interface promoted ammonia selectivity and kinetics [21]. These results show that MXenes do more than serve as conductive supports; they also influence interfacial electronics and reaction pathways. Experimental conditions and synthesis complexity have so far restricted studies to a small number of systems. Key parameters (MXene substrate, supported metal, and anchoring site) have not been systematically varied or compared.

First-principles calculations have begun to clarify structure–activity relations for MXene-based NO_3RR catalysts [22]. Theoretical calculations show that nitrate reduction activity and selectivity depend

strongly on the MXene substrate [23]. The substrate is therefore not a passive scaffold; it shapes catalytic behavior. Calculations also show that transition-metal single atoms on MXenes alter surface electronic structure and intermediate adsorption and desorption [24]. Most of these studies, however, treat isolated systems. Few compare different substrate–single-atom pairs under identical computational settings. How the MXene lattice and single-atom site cooperate remains unclear. Intrinsic metal properties, including electronegativity and atomic radius, introduce further complexity. How they combine to set intermediate adsorption free energies and overall activity is still poorly understood.

First-principles calculations are now widely used to study NO_3RR mechanisms and to screen catalysts [25]. The search space, however, is enormous. It involves many substrates, single-atom metals, and adsorption sites. Conventional point-by-point density functional theory (DFT) calculations therefore struggle to cover all potential candidates efficiently [26,27]. To address this challenge, machine learning (ML) methods have been increasingly introduced into catalytic research, with their application focus gradually shifting from the early stage of "accelerating virtual screening" toward the "elucidation of catalytic activity origins" [28,29]. Earlier studies used DFT-derived structural and electronic properties as descriptors in ML models to establish quantitative structure–activity relationships [30,31]. These descriptors include formation energy, adsorption energy, the d-band center, intrinsic atomic properties, and local geometric parameters. Most models, however, rely on empirically chosen descriptors. Their physicochemical interpretation and relationship to catalytic activity often remain unclear [32,33]. In addition, systematic evaluations of the electrochemical stability of catalysts under realistic operating conditions and their selectivity toward competing reactions (such as HER) remain insufficient.

To address the aforementioned challenges, this study employs DFT calculations to construct a series of MXene-based SAC models (TM@M_2CO_2, where TM denotes the anchored transition-metal atom and M represents Mo, W, or Cr), in which the TM atoms are anchored at the face-centered cubic (fcc) and hexagonal close-packed (hcp) hollow sites on Mo_2CO_2, W_2CO_2, and Cr_2CO_2 MXene substrates [34–37]. We then used the DFT results to screen candidates stepwise: thermodynamic stability first, electrochemical stability second, and reaction selectivity third. This process narrowed the pool to the most promising candidates under the computational framework adopted here. Subsequently, focusing on the limiting potential (U_L) as the key activity descriptor, detailed reaction mechanism and kinetic analyses were conducted for the optimized systems. Finally, regression models were compared using leave-one-out cross-validation (LOOCV) and five-fold cross-validation (5-fold CV) to assess internal predictive performance within the screened dataset. Feature-importance and Shapley Additive Explanations (SHAP) analyses were used to explore descriptor–activity associations. The objective is to combine DFT-based catalyst screening and mechanistic analysis with exploratory data-driven interpretation, providing hypotheses for the further design and investigation of MXene-based NO_3RR catalysts.

2. Methods

All initial structures were constructed using the Materials Studio software [38]. Three O-terminated MXene substrates, namely Mo_2CO_2, W_2CO_2, and Cr_2CO_2, were selected as representative MXene-based supports. A 3 × 3 × 1 supercell was employed for each substrate, and TMs from groups IV, V, and VI were subsequently anchored at the fcc and hcp threefold hollow sites of the substrate surface to construct a series of MXene-based SAC models (see Figure 1). For clarity, the fcc and hcp sites were denoted as site I and site II, respectively; the substrate metal was represented by M, while the supported single-atom

metal was denoted as TM. All catalysts are uniformly labeled as TM@M_2CO_2 (e.g., RuI@Mo_2CO_2). To avoid interlayer mirror interactions, a sufficiently thick vacuum layer of 20 Å was introduced along the z direction perpendicular to the surface. All models were fully geometrically optimized to obtain stable configurations.

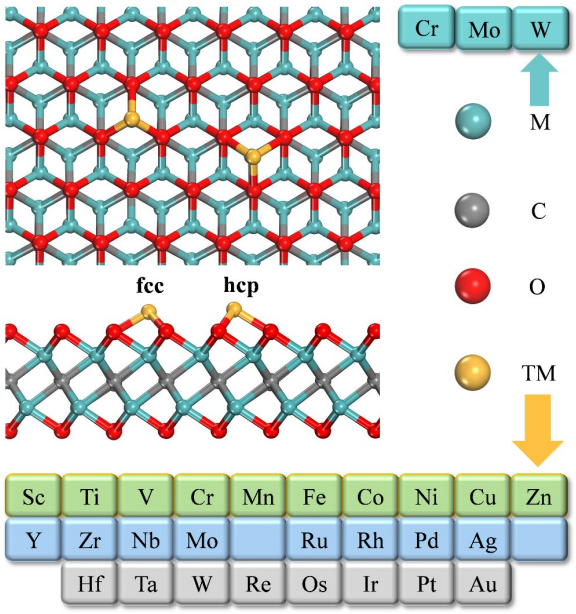


Figure 1. Structural models of MXene-supported TM@M_2CO_2 SACs.

DFT calculations were performed using the DMol^3 module implemented in Materials Studio software [38]. The electronic exchange–correlation energy was described using the Perdew–Burke–Ernzerhof (PBE) functional within the framework of the generalized gradient approximation (GGA) [39–41]. The long-range dispersion interactions were corrected using the Grimme PBE-D3 method [42]. The density functional semi-core pseudopotential (DSPP), which considers relativistic effects, was employed to describe the ionic potentials, while the valence electron wave functions were expanded using a double numerical basis set with polarization functions (DNP) [43]. A Fermi smearing of 0.001 Ha was applied in the numerical calculations to ensure convergence accuracy [44]. Geometry optimizations used an energy tolerance of 1×10^{-5} Ha; the maximum force and displacement thresholds were 2×10^{-3} Ha·Å^{-1} and 5×10^{-3} Å, respectively. Brillouin-zone integration used a 6 × 6 × 1 Monkhorst–Pack k-point mesh. TM active centers may host unpaired d electrons. Spin-polarized calculations were therefore adopted for all systems, allowing the spin-up and spin-down densities to relax independently during the self-consistent field iterations [45]. This approach ensures that the calculated total energies, adsorption free energies, and reaction free energies were obtained based on spin-polarized ground states, thereby incorporating possible local magnetic contributions into the energy evaluation. To account for solvent effects, the conductor-like screening model (COSMO) was employed to simulate the H_2O solvent environment with a dielectric constant of 78.54 [46,47].

We calculated the formation energy (E_f) as:

$$E_f = E_{TM@MXene} - E_{MXene} - \mu_{TM} \quad (1)$$

where $E_{TM@MXene}$ represents the total energy of the system after anchoring the TM atom, E_{MXene} denotes the total energy of the pristine MXene substrate, and μ_{TM} is the chemical potential of the single-atom metal TM (defined as the energy per atom of the corresponding bulk metal in this work).

The dissolution potential (U_{diss}) was employed as a thermodynamic descriptor to evaluate the electrochemical dissolution tendency of the anchored TM atom. It represents the thermodynamic driving force associated with the removal of the supported TM atom from the MXene substrate into the dissolved state. The dissolution potential (U_{diss}) was defined as follows:

$$U_{diss} = U_{diss}^{0} - \frac{E_f}{Ne} \quad (2)$$

where U_{diss}^{0} is the standard dissolution potential of the corresponding bulk metal, E_f is the formation energy of the anchored single-atom system, and N represents the number of electrons transferred during the metal dissolution process, and e is the elementary charge. The standard dissolution potentials U_{diss}^{0} of the investigated TMs and the number of N were both obtained from the CRC handbook of chemistry and physics [48]. All corresponding numerical values used in this work are compiled in Table S1 of the supporting information.

The adsorption free energy of NO_3^- (ΔG_{*NO_3}) was defined as follows:

$$\Delta G_{*NO_3} = G_{*NO_3} - G_{*} - G_{HNO_3(g)} + 1/2G_{H_2(g)} + \Delta G_{correct\ (1)} \quad (3)$$

where G_{*NO_3} represents the Gibbs free energy of the system after adsorption of NO_3^-, G_* denotes the Gibbs free energy of the pristine catalyst substrate, and $G_{HNO_3(g)}$ and $G_{H_2(g)}$ are the Gibbs free energies of gaseous HNO_3 and H_2, respectively. $\Delta G_{correct\ (1)}$ represents the correction term applied to account for additional contributions not included in the DFT total energy, which was set to 0.392 eV [49,50].

The adsorption free energy of H^+ (ΔG_{*H}) was defined as follows:

$$\Delta G_{*H} = G_{*H} - G_{*} - 1/2G_{H_2(g)} + \Delta G_{correct\ (2)} \quad (4)$$

where G_{*H} represents the total energy of the system after proton adsorption, and $\Delta G_{correct\ (2)}$ is the correction term, which was set to 0.24 eV [51].

The computational hydrogen electrode (CHE) model was employed to calculate the Gibbs free energy changes (ΔG) for each elementary reaction step, which were determined according to the following equation:

$$\Delta G = \Delta E + \Delta ZPE - T\Delta S + \Delta G_U + \Delta G_{pH} \quad (5)$$

where ΔE is the reaction energy difference obtained from DFT calculations. ΔZPE and ΔS represent the changes in zero-point energy and entropy before and after adsorption at 298 K, respectively, which were derived from the vibrational frequencies calculated by DFT. $\Delta G_U = -eU$ represents the potential-dependent Gibbs free-energy correction introduced by the applied electrode potential U. ΔG_{pH} is the pH correction term, defined as $\Delta G_{pH} = k_B T \times pH \times \ln 10$, where k_B is the Boltzmann constant, T is the temperature, and pH represents the acidity of the electrolyte. All Gibbs free-energy calculations in this work were performed under acidic conditions with pH = 0. Accordingly, the pH-dependent correction was set to $\Delta G_{pH} = 0$.

The U_L was defined as the minimum electrode potential required to make all elementary reaction steps exothermic ($\Delta G \leq 0$), and it was calculated according to the following equation:

$$U_L = -\Delta G_{max}/e \quad (6)$$

Here, ΔG_{max} is the largest Gibbs free energy change among the elementary steps. These steps lie along the most favorable reaction pathway.

ML model predictions were assessed with three metrics: the coefficient of determination (R^2), mean absolute error (MAE), and root mean square error (RMSE). Their corresponding expressions are as follows:

$$R^2 = 1 - \frac{\sum_{i=1}^{n}(y_i - \hat{y}_i)^2}{\sum_{i=1}^{n}(y_i - \bar{y})^2} \quad (7)$$

Here, y_i is the actual value, $\hat{y}_i$ is the predicted value, and $\bar{y}$ is the mean value of the actual value. A value of R^2 closer to 1 indicates a stronger explanatory capability of the model for the target variable.

$$MAE = \frac{1}{n}\sum_{i=1}^{n}|y_i - \hat{y}_i| \quad (8)$$

MAE reflects the average absolute deviation between the predicted values and the actual values, where a smaller value indicates higher prediction accuracy.

$$RMSE = \sqrt{\frac{1}{n}\sum_{i=1}^{n}(y_i - \hat{y}_i)^2} \quad (9)$$

RMSE is more sensitive to larger prediction errors and can be used to comprehensively evaluate the prediction stability of the model. A smaller RMSE value indicates better model performance.

3. Results and discussion

3.1. Stability screening

In this study, three O-terminated MXenes, namely Cr_2CO_2, Mo_2CO_2, and W_2CO_2, were selected as anchoring substrates. A total of 26 TM atoms from groups IV, V, and VI were individually anchored at the surface fcc and hcp threefold hollow sites to construct a series of MXene-based SAC models, as illustrated in Figure 1. Among the selected TM elements, Cd was excluded due to its fully occupied $4d^{10}5s^2$ electronic configuration, which results in insufficient catalytic activity, as well as its well-documented biological toxicity [52]. Meanwhile, Tc was also excluded because of its radioactivity and extreme scarcity, which would lead to high operational costs and potential safety hazards [53]. Both elements contradict the principles of selecting efficient and environmentally friendly catalysts [54]. We did not choose anchored TM atoms identical to the substrate metals. This avoids ambiguity in identifying active sites and helps keep the single atoms stably dispersed. Consequently, 150 theoretical TM@M_2CO_2 systems were constructed for subsequent investigations (Figure 1).

The anchoring stability of single atoms on MXene surfaces was evaluated from both thermodynamic and electrochemical perspectives. The thermodynamic stability was determined by the formation energy (E_f), while the dissolution potential (U_{diss}, defined in Section 2) was employed as a thermodynamic descriptor for electrochemical stability. Within the adopted model, a positive U_{diss} indicates that the dissolution of the anchored TM atom is thermodynamically unfavorable relative to the corresponding bulk-metal

reference state, and thus $U_{diss} > 0$ is used as a preliminary criterion for electrochemical stability screening. It should be noted that U_{diss} is based on a simplified thermodynamic description referenced to the corresponding bulk-metal state and therefore does not fully represent the dynamic behavior of SACs under realistic electrochemical conditions. In particular, the present treatment does not explicitly account for changes in TM–MXene interactions induced by adsorbed reaction intermediates, nor does it consider possible MXene surface reconstruction, oxidation, or other environment-dependent structural changes. Therefore, $U_{diss} > 0$ should be interpreted as an indication of favorable thermodynamic stability within the adopted computational model rather than as a guarantee that the single atom will resist dissolution in a real electrolyte.

A stable material should satisfy the criteria of $E_f < 0$ and $U_{diss} > 0$. The scatter plot of E_f and U_{diss} for the 150 calculated materials is presented in Figure 2, with the corresponding numerical values summarized in Tables S2–S4. As shown in Figure 2, except for the following 11 systems, ZnI@Mo_2CO_2, ZnII@Mo_2CO_2, PtII@Mo_2CO_2, NiII@Mo_2CO_2, ZnI@W_2CO_2, ZnII@W_2CO_2, PtII@W_2CO_2, NiII@W_2CO_2, ZnI@Cr_2CO_2, ZnII@Cr_2CO_2, and PtII@Cr_2CO_2, all other systems exhibit negative formation energies. For most systems studied, single-metal anchoring is thermodynamically favorable. Formation-energy screening left 139 materials. Of these, 26 had negative dissolution potentials (Figure 2 and Tables S2–S4). Under the adopted model, this indicates a thermodynamic driving force for dissolution, so these systems were excluded as thermodynamically unstable. The remaining 113 materials met both the thermodynamic and electrochemical stability criteria and were selected for further study.

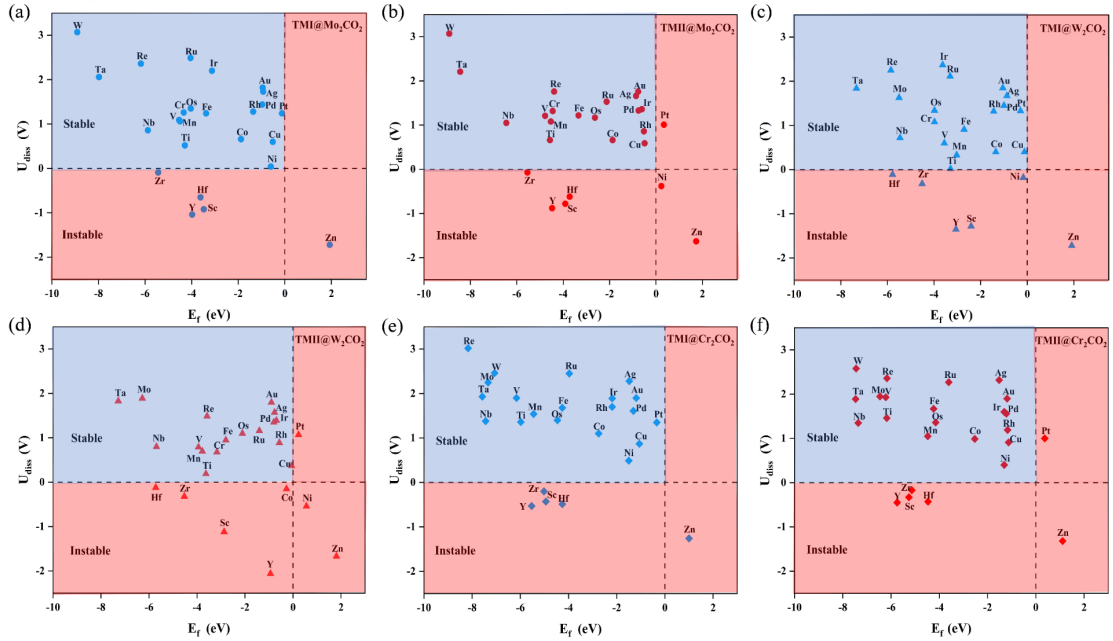


Figure 2. Scatter plots showing the distribution of formation energy (E_f) and dissolution potential (U_{diss}) on TM@M_2CO_2. **(a)** fcc site of Mo_2CO_2; **(b)** hcp site of Mo_2CO_2; **(c)** fcc site of W_2CO_2; **(d)** hcp site of W_2CO_2; **(e)** fcc site of Cr_2CO_2; **(f)** hcp site of Cr_2CO_2. Blue symbols correspond to the fcc sites, and red symbols to the hcp sites.

3.2. Selectivity screening

During NO_3RR, the HER is the most significant competing side reaction, originating from the competitive adsorption of H^+ and NO_3^- at the catalyst active sites [55]. To suppress HER, the catalyst

must bind NO_3^- more strongly than H^+. In free-energy terms, ΔG_{*NO_3} should be more negative than ΔG_{*H}. When $\Delta G_{*NO_3} < \Delta G_{*H}$, NO_3^- is preferentially activated, satisfying the selectivity criterion [25].

In real electrolytes, NO_3RR depends on a continuous H^+ supply. HER interference is therefore difficult to avoid completely. The criterion $\Delta G_{*NO_3} < \Delta G_{*H}$ alone is not enough to assess overall catalytic performance. According to the Sabatier principle, an excessively negative ΔG_{*NO_3} value (indicating overly strong adsorption) may suppress HER but simultaneously poison the active sites and hinder the desorption of subsequent reaction intermediates, ultimately reducing the overall reaction rate. Therefore, a comprehensive evaluation of selectivity must not only consider HER suppression but also ensure that nitrate adsorption is neither too strong nor too weak. Specifically, we adopt the following dual criterion: (i) ensuring $\Delta G_{*NO_3} < \Delta G_{*H}$ to resist HER competition; and (ii) restricting ΔG_{*NO_3} within an appropriate adsorption energy window based on the Sabatier principle, thereby guaranteeing effective regeneration of active sites and smooth catalytic cycles.

To assess competitive adsorption between NO_3^- and H^+, we calculated adsorption free energies for all 113 systems. Figure 3 summarizes these results. The numerical values are given in Tables S5–S7. The dashed diagonal denotes $\Delta G_{*NO_3} = \Delta G_{*H}$. Systems above this line in the light-green region satisfy $\Delta G_{*NO_3} < \Delta G_{*H}$ and thus favor nitrate adsorption. Those below the line in light purple prefer H^+ adsorption instead. Both the MXene substrate and the coordination environment of the anchored TM atoms affect where these points lie. The criterion $\Delta G_{*NO_3} < \Delta G_{*H}$ initially identified 65 candidates. Some of them, however, bind NO_3^- too strongly, which would hinder intermediate conversion and product desorption. Further screening thus needs an additional constraint on adsorption strength.

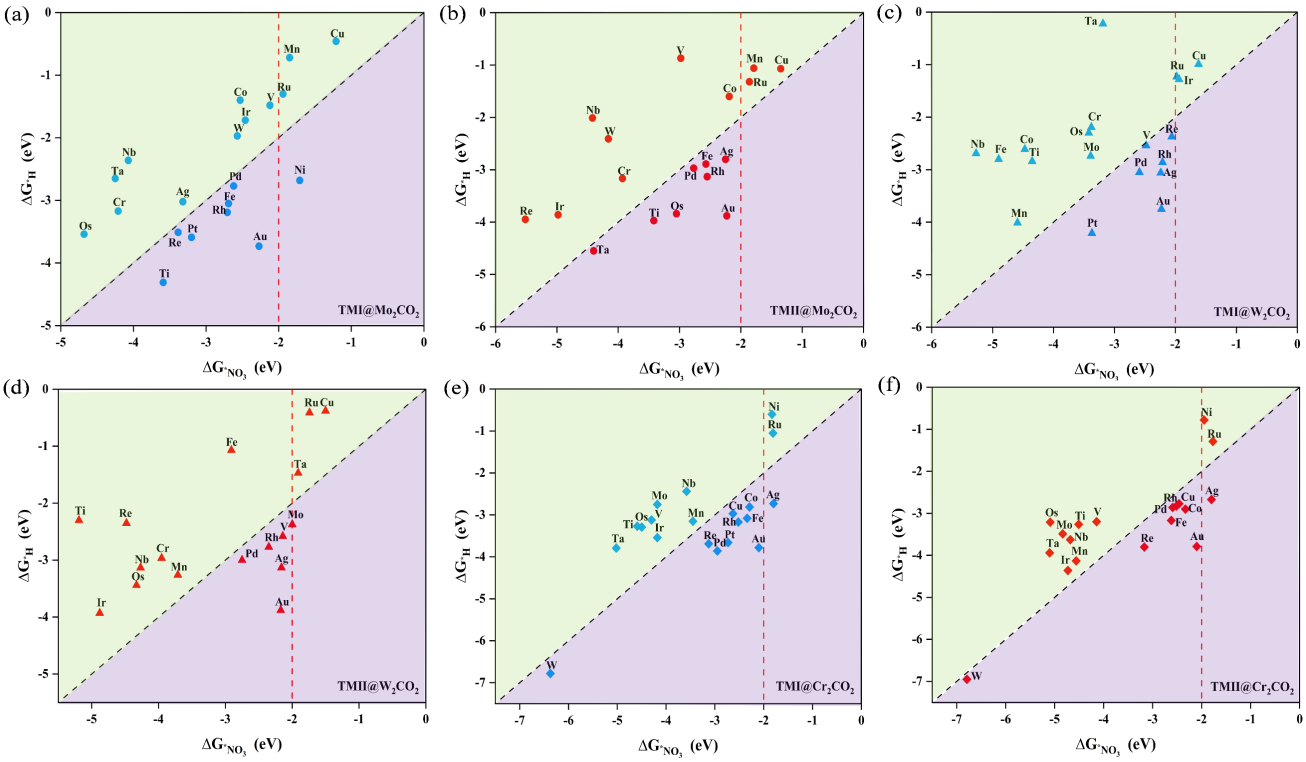


Figure 3. Scatter distribution of nitrate adsorption energy (ΔG_{*NO_3}) and hydrogen adsorption energy (ΔG_{*H}) on TM@M_2CO_2. **(a)** fcc site of Mo_2CO_2; **(b)** hcp site of Mo_2CO_2; **(c)** fcc site of W_2CO_2; **(d)** hcp site of W_2CO_2; **(e)** fcc site of Cr_2CO_2; **(f)** hcp site of Cr_2CO_2. Blue symbols correspond to the fcc sites, and red symbols to the hcp sites.

According to the Sabatier principle, a catalyst performs best when key intermediates bind neither too strongly nor too weakly [56]. The ΔG_{*NO_3} window of −2 to 0 eV was adopted as an empirical criterion for preliminary high-throughput screening based on previously reported nitrate reduction and Sabatier-principle studies [56,57]. The upper limit of 0 eV ensures sufficiently favorable nitrate adsorption, whereas the lower limit of −2 eV is intended to exclude systems with excessively strong nitrate binding, for which the Brønsted–Evans–Polanyi (BEP) relation predicts systematically higher hydrogenation barriers and impeded product release. We took this lower limit from the literature as a conservative threshold. It is not derived from first-principles calculations. A sensitivity analysis varying the lower limit from −1.5 to −3.0 eV shows that the number of selected systems changes from 3 (−1.5 eV) to 16 (−2.0 eV) to 19 (−2.5 eV) to 23 (−3.0 eV) (Table S8). CuI@Mo_2CO_2 (−1.21 eV) remains selected over the whole range, while RuII@W_2CO_2 (−1.74 eV) is filtered out only at the strictest limit of −1.5 eV. Both candidates are retained for lower limits of −2.0 eV and more negative. Because RuII@W_2CO_2 is one of the two best-performing candidates, the −1.5 eV limit is too restrictive and would introduce a significant false negative, whereas limits of −2.5 and −3.0 eV retain both candidates but enlarge the candidate pool substantially. The −2 eV limit therefore represents a reasonable compromise between avoiding false negatives and maintaining screening efficiency. In particular, three systems with ΔG_{*NO_3} between −2.0 and −2.5 eV (VI@Mo_2CO_2, IrI@Mo_2CO_2, and CoII@Mo_2CO_2) are excluded only by the −2.0 eV limit and are documented in Table S8 for completeness. This range should therefore be read as a screening window, not a universal thermodynamic boundary for NO_3RR activity. In particular, catalysts with ΔG_{*NO_3} slightly below −2 eV may still exhibit competitive activity because the overall catalytic performance is determined by the complete free-energy landscape rather than by nitrate adsorption strength alone. We used the −2 to 0 eV window only as a conservative screening filter, not as a definitive activity criterion. Because this cutoff is empirical, it may miss some active systems and produce false negatives. Screening with this criterion gave 16 candidates for further study: MnI@Mo_2CO_2, CuI@Mo_2CO_2, RuI@Mo_2CO_2, MnII@Mo_2CO_2, CuII@Mo_2CO_2, RuII@Mo_2CO_2, CuI@W_2CO_2, RuI@W_2CO_2, IrI@W_2CO_2, TaII@W_2CO_2, CuII@W_2CO_2, RuII@W_2CO_2, NiI@Cr_2CO_2, RuI@Cr_2CO_2, NiII@Cr_2CO_2, and RuII@Cr_2CO_2. These 16 systems are a starting point for further calculations, not a complete list of every TM@M_2CO_2 catalyst that might be active.

The selectivity screen in this work uses two thermodynamic adsorption free energies, ΔG_{*NO_3} and ΔG_{*H}. These are computationally inexpensive and physically meaningful, so they serve as a first-order criterion for high-throughput screening. The rationale is straightforward: NO_3^- and H^+ compete for surface sites, and their relative binding strength largely controls which species occupies a site and becomes activated. A negative ΔG_{*NO_3}, together with $\Delta G_{*NO_3} < \Delta G_{*H}$, ensures that nitrate can preferentially occupy active sites and be activated. This is a necessary but not sufficient thermodynamic prerequisite for suppressing HER. A full climbing-image nudged elastic band (CI-NEB) screen of all candidates was not feasible. There are 150 systems, and transition-state searches are expensive. Running CI-NEB for every candidate at the screening stage would be computationally prohibitive. Thermodynamic adsorption energies alone also cannot capture the full kinetics of the competing network. Actual selectivity depends on the interplay between the activation barrier of the NO_3RR PDS and those of the HER Volmer/Tafel steps, as well as coverage effects, interfacial solvent reorganization, and electrode-potential dependence. The thermodynamic screen is therefore a preliminary filter for promising candidates, not a definitive prediction

of kinetic selectivity. Explicit CI-NEB calculations were later performed for the two top-performing catalysts to provide kinetic verification (Section 3.3).

3.3. Performance of NO_3RR

NO_3RR produce NH_3, along with byproducts such as NO_2^- and N_2. As shown in Figure 4, NO_3RR can be mainly classified into O-end adsorption, N-side adsorption, O-side hydrogenation, N-side hydrogenation, and NO dimerization (NO-dimer) pathways, depending on the adsorption configurations of intermediates and the proton attack sites during the hydrogenation.

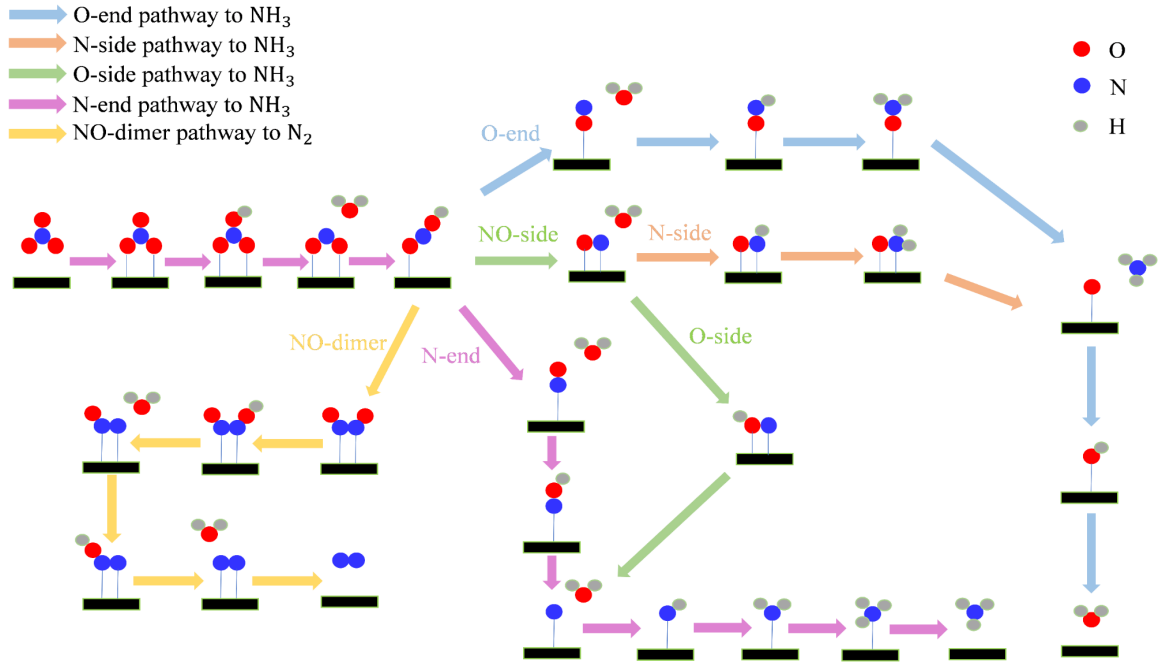


Figure 4. Reaction network diagram of nitrate reduction reaction.

Previous studies have demonstrated that NH_3 is the thermodynamically favored product under negative electrode potentials [50]. Therefore, this study focuses on the NH_3 formation pathway. As shown in Figure 4, after NO_3^- is hydrogenated–dehydrated to $*NO_2H$, its further conversion to *NO can follow three competing pathways (O-end, NO-side, N-end), depending on the adsorption configuration of *NO [50,58]. The Gibbs free-energy changes associated with the O-end, NO-side, N-end, and NO-dimer pathways for the 16 candidate catalysts are summarized in Table S9. Among the three considered configurations leading to *NO, the N-end configuration exhibits the most favorable free-energy change in all 16 systems, and the NO-dimer pathway is consistently less favorable than the N-end pathway. These results support the relative thermodynamic preference for the N-end pathway over the considered competing pathways within the adopted computational model. Moreover, since *NO protonation can occur at either the N or O site, both *NHO and *NOH configurations were considered. Their ΔG values were compared to determine the thermodynamically preferred pathway, which was then adopted for subsequent NO_3RR analysis [59,60].The ΔG values for forming these intermediates over the 16 systems are listed in Table S10. Following this strategy, Table S11 summarizes the calculated Gibbs free energy changes for all elementary steps of the NO_3RR pathway over the 16 $TM@M_2CO_2$ catalysts. The U_L calculations were further calculated for the 16 candidate systems and the results are presented in Figure 5. Among these materials, $CuI@Mo_2CO_2$

and RuII@W_2CO_2 are predicted to exhibit the most favorable catalytic performance, with U_L values of −0.38 V and −0.45 V (relative to the reversible hydrogen electrode, RHE), respectively. These results indicate that, within the adopted computational model, both catalysts possess low overpotential requirements and are theoretically promising for NO_3RR catalysis. Therefore, these two structures were selected for further in-depth mechanistic investigations.

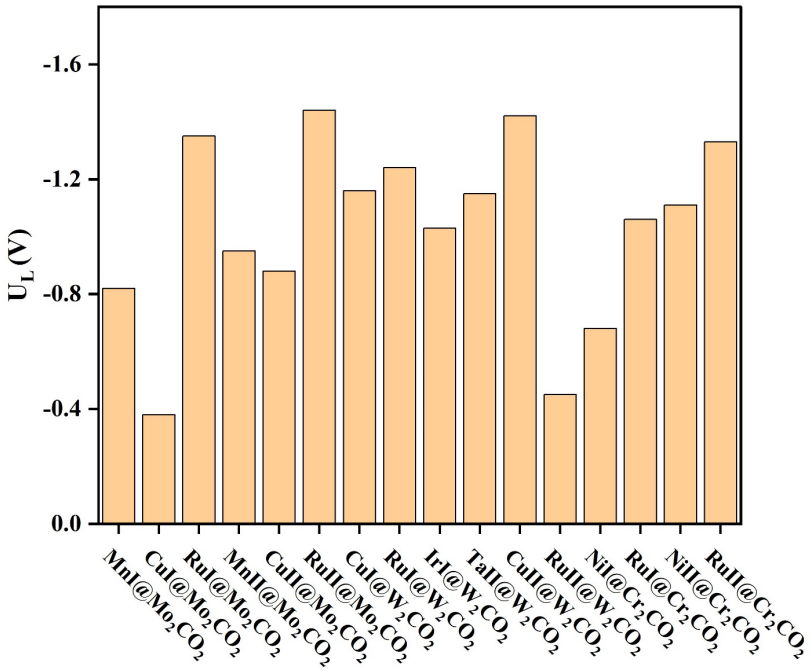


Figure 5. U_L values for the 16 TM@M_2CO_2 systems.

To further evaluate the thermodynamic feasibility, we present the complete NO_3RR free-energy profiles for CuI@Mo_2CO_2 and RuII@W_2CO_2 in Figure 6, and for the remaining 14 catalysts in Figures S1–S14. The reaction initiates with the chemical adsorption of NO_3^- on the catalyst surface, with adsorption free energies of −1.21 eV and −1.74 eV on CuI@Mo_2CO_2 and RuII@W_2CO_2, respectively, indicating that NO_3^- can be stably anchored and effectively activated. Subsequently, the adsorbed *NO_3 undergoes the first proton-coupled electron transfer (PCET) step to generate *NO_3H. Under the adopted acidic condition (pH = 0), this step exhibits the highest thermodynamic energy barrier on CuI@Mo_2CO_2 (ΔG = 0.38 eV) and thus is identified as the potential-determining step (PDS) of this catalyst. For RuII@W_2CO_2, however, under the adopted acidic condition (pH = 0), the PDS occurs at a later stage (the hydrogenation of *NO to *NHO, see below), while the *NO_3 → *NO_3H step is highly exergonic with a Gibbs free energy change of −2.08 eV. On CuI@Mo_2CO_2 and RuII@W_2CO_2, *NO_3H subsequently undergoes proton attack and the elimination of one H_2O molecule to form *NO_2, with the corresponding Gibbs free energies changes of −1.46 eV and −2.63 eV, respectively. The hydrogenation of *NO_2 to form *NO_2H results in Gibbs free energy changes of −1.66 eV for CuI@Mo_2CO_2 and −2.57 eV for RuII@W_2CO_2. *NO_2H loses a second water molecule, leaving *NO adsorbed on both catalysts in an N-end configuration. This dehydration is downhill on RuII@W_2CO_2 (ΔG = −0.74 eV), but costs an extra 0.29 eV on CuI@Mo_2CO_2. Further protonation gives *NHO. At pH=0, this step is the PDS on RuII@W_2CO_2, with a thermodynamic barrier of 0.45 eV. On CuI@Mo_2CO_2, the same protonation is strongly exergonic (ΔG = −2.09 eV). After *NHO forms, hydrogenation proceeds step by step,

and NH_3 desorbs at the end. On both catalysts, free energy keeps falling along these steps. They are therefore spontaneous.

It should be noted that the above free-energy profiles, U_L, and PDS assignments were obtained under the adopted acidic condition of pH = 0. Because the pH-dependent correction (ΔG_{pH}) directly affects PCET steps, changes in pH can modify the relative free energies of reaction intermediates and consequently alter the U_L, PDS, and even the relative thermodynamic preference of competing reaction pathways. Therefore, the U_L, PDS assignments, dominant reaction pathways, and the ranking of the screened candidates identified in this work are specific to the adopted acidic conditions and should not be directly generalized to neutral or alkaline NO_3RR conditions.

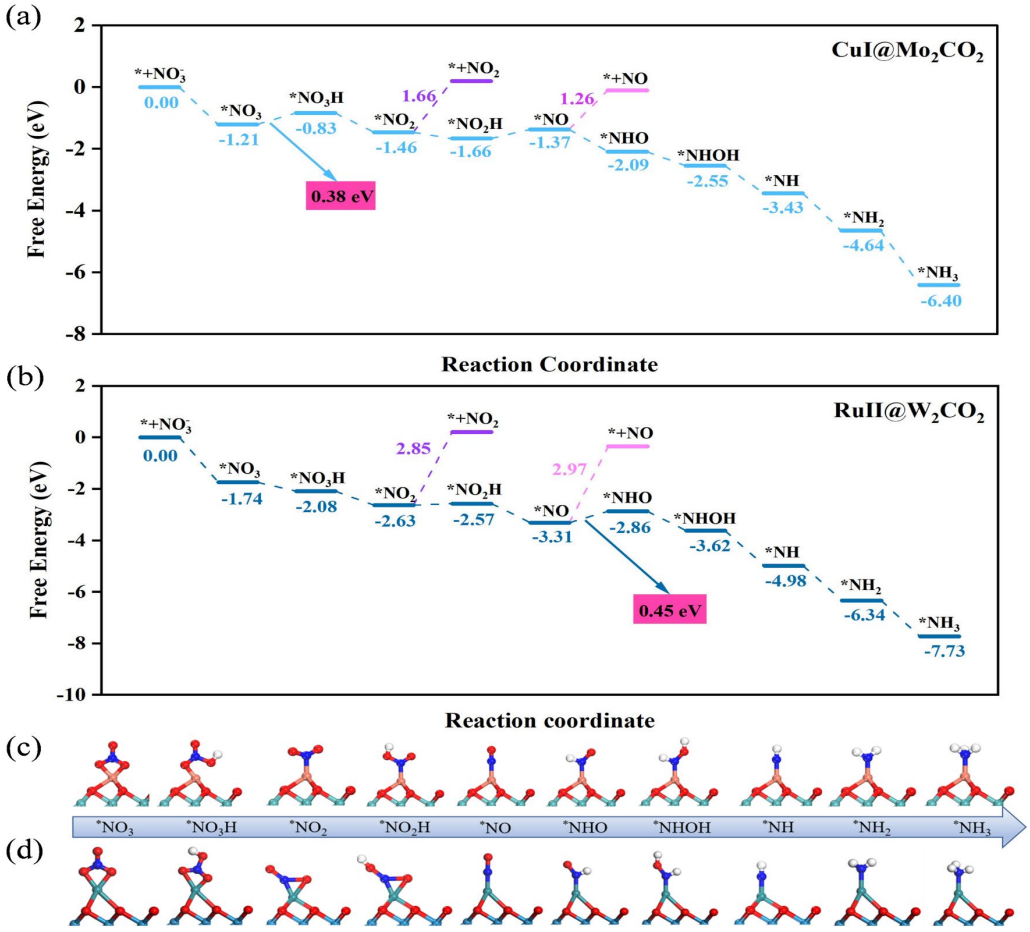


Figure 6. Free energy diagrams of the optimal NO_3RR pathway on **(a)** CuI@Mo_2CO_2 and **(b)** RuII@W_2CO_2. Adsorption configurations of NO_3RR intermediates on **(c)** CuI@Mo_2CO_2 and **(d)** RuII@W_2CO_2. Red, white, dark blue, orange, light green, green, and blue atoms represent O, H, N, Cu, Mo, Ru, and W, respectively.

To further elucidate the kinetic feasibility and rate-determining nature of the NO_3RR pathways, the CI-NEB method was employed to search for the transition states of the PDS steps on the two catalysts, thereby determining their activation energy barriers. The results are shown in Figure 7. For CuI@Mo_2CO_2 (Figure 7a), the activation energy barrier (E_a) for the hydrogenation of *NO_3 to form *NO_3H (PDS) is 0.57 eV. This kinetic barrier is highly consistent with the thermodynamic energy requirement of this step (ΔG = 0.38 eV) and the limiting potential (U_L = − 0.38 V), fully validating the agreement between kinetic and thermodynamic descriptions in identifying the rate-determining step

within the CHE model framework. For RuII@W_2CO_2 (Figure 7d), the PDS corresponds to the hydrogenation of *NO to generate *NHO, with an activation energy barrier of 0.72 eV. This value is also consistent with its thermodynamic barrier (0.45 eV) and limiting potential (−0.45 V). These results not only confirm the thermodynamic feasibility of the nitrate reduction pathways on both catalysts but also demonstrate their kinetic accessibility. Among them, CuI@Mo_2CO_2 is predicted to exhibit superior kinetic performance due to its lower reaction energy barrier compared with RuII@W_2CO_2.

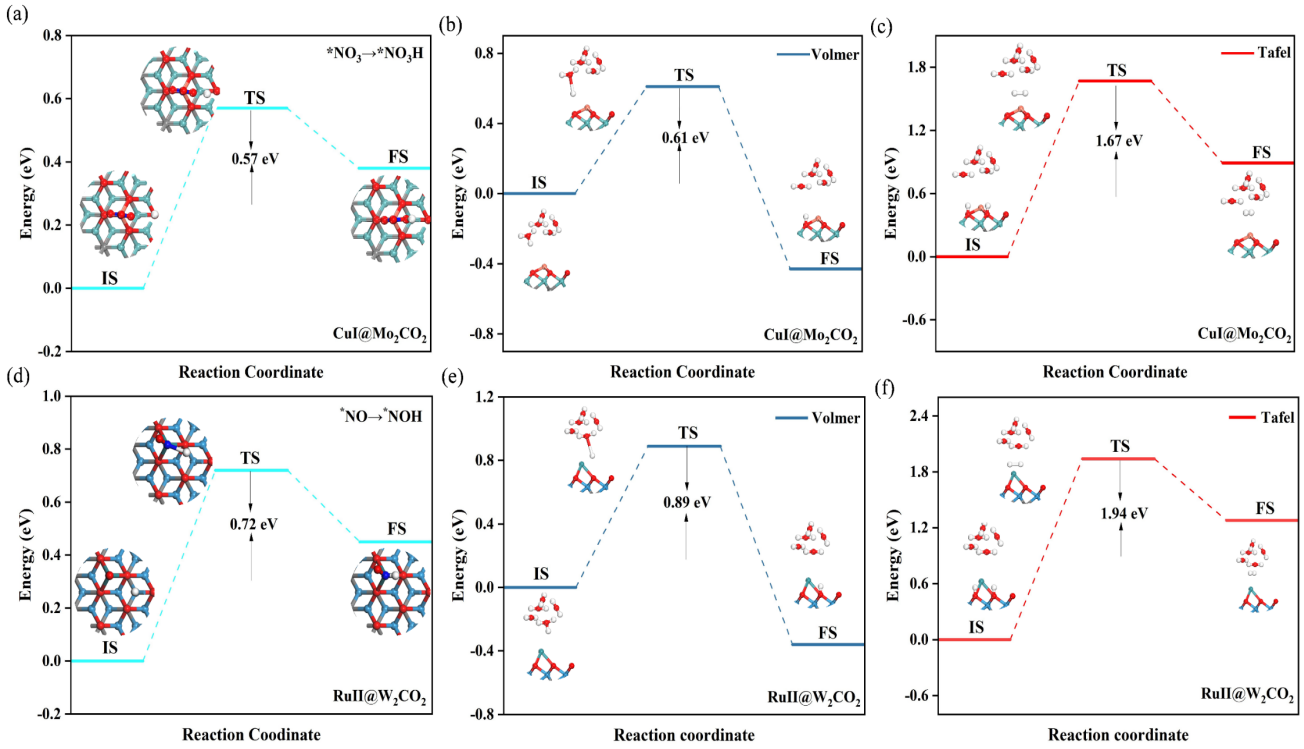


Figure 7. Energy profiles and corresponding activation barriers for the potential-determining steps of the NO_3RR and the competing HER on CuI@Mo_2CO_2 **(a–c)** and RuII@W_2CO_2 **(d–f)** catalysts. IS, TS and FS represent the initial state, transition state, and final state, respectively.

Beyond the activity of the target reaction, selectivity is also a critical indicator for evaluating electrocatalytic performance. To further verify the selectivity of the two materials toward NO_3RR over HER, the HER kinetic barriers were systematically evaluated through the Volmer–Tafel pathway. As shown in Figure 7b, c, on CuI@Mo_2CO_2, the activation energy barrier of the Volmer step ($* + H^+ + e^- \rightarrow H$) is 0.61 eV, which is higher than that of the NO_3RR PDS (0.57 eV). On CuI@Mo_2CO_2, the Tafel step ($2H \rightarrow H_2 + *$) has a barrier of 1.67 eV (Figure 7e). Recombination and desorption of adsorbed H are therefore kinetically unfavorable. RuII@W_2CO_2 shows the same pattern (Figure 7f). Its Volmer barrier is 0.89 eV, well above the NO_3RR PDS (0.72 eV). The Tafel barrier is higher still, at 1.94 eV. On both catalysts, protons preferentially hydrogenate nitrate rather than recombine into H_2. Under the adopted computational conditions, HER is kinetically suppressed relative to NO_3RR. NO_3RR should therefore be more selective than HER in theory.

CI-NEB kinetic validation covered only CuI@Mo_2CO_2 and RuII@W_2CO_2, the two most promising candidates. The other 14 shortlisted systems were not tested. Mapping all transition states along the full multi-step NO_3RR and HER networks on 16 surfaces would require far too many CI-NEB calculations. The thermodynamic criterion in Section 3.2 is necessary for high selectivity, but not sufficient. For the

remaining 14 candidates, $\Delta G_{*NO_3} < \Delta G_{*H}$ is an early sign that HER is suppressed. It does not prove kinetic selectivity. Explicit barriers are still needed. Keep this in mind when reading the screening results. Mapping kinetics across all candidates will need ML-accelerated transition-state searches or microkinetic modeling.

We also checked whether nitrogen-containing byproducts could compete. We examined NO_2-derived intermediates, molecular NO_2 desorption, and the NO-dimer pathway. $*NO_2$ hydrogenation to $*NO_2H$ is exergonic on CuI@Mo_2CO_2 (−0.20 eV) and nearly thermoneutral on RuII@W_2CO_2 (+0.06 eV) (Figure 6 and Table S11). Adsorbed $*NO_2$ can therefore continue along the nitrate reduction pathway rather than build up as a terminal surface species. Molecular NO_2 desorption is thermodynamically unfavorable for all 16 shortlisted systems. The positive free-energy changes range from 1.66 to 2.85 eV (Figure 6 and Figures S1–S14). On all 16 systems, the NO-dimer pathway has higher free-energy changes than the corresponding N-end pathway (Table S9). N-end hydrogenation is therefore favored over the N-N coupling route considered here. Taken together, within the surface pathways examined here, these byproduct routes are not thermodynamically dominant relative to the N-end hydrogenation pathway.

What we calculate is the hydrogenation of adsorbed $*NO_2$. That is not the same as forming or accumulating dissolved nitrite (NO_2^-). We do not explicitly calculate NO_2^- formation or its release into the electrolyte. Solution-phase nitrite concentration, mass transport, and potential-dependent desorption are also outside the present model. The energetics therefore help explain the relative favorability of the surface pathways studied here. They do not show that nitrite accumulation or every possible byproduct is fully suppressed. Our conclusions are limited to the pathways explicitly examined in this study.

The calculations suggest CuI@Mo_2CO_2 and RuII@W_2CO_2 are promising for NO_3RR. Both are thermodynamically and kinetically favorable. Under the conditions used here, HER is suppressed on both. They are therefore worth considering as theoretical electrocatalysts for nitrate reduction. Notably, the U_L of CuI@Mo_2CO_2 (−0.38 V) surpasses those of recently reported Tc@Ov-W_2CO_2 (−0.42 V) [61], V@Ti_2NO_2 (−0.41 V) [62], Cr@Ti_2NO_2 (−0.52 V) [63], and anti-MXene borides OsB (−0.66 V) and FeB (−0.70 V) [63], as illustrated in Figure 8.

Figure 8 compares U_L values taken from different theoretical studies. The computational protocols differ, so the reported values differ too. The exchange-correlation functional is one source. It changes the calculated adsorption energies and, through them, the free-energy changes of the elementary steps that set U_L. The magnitude and direction of this effect depend on the adsorbate and the catalyst surface [64,65]. Solvation models are a second source. Solvent polarization and hydrogen bonding can change how stable adsorbed intermediates are. That changes the reaction free energies and can shift U_L [66]. Differences in CHE implementation, thermodynamic corrections, and reference states can also affect the calculated free-energy profiles and U_L [51]. Here, the CHE correction and reference-state conventions are stated in the Methods section. Figure 8 is therefore a qualitative comparison with representative 2D NO_3RR catalysts, including previously reported MXene and anti-MXene boride monolayers. It is not a strict quantitative ranking of studies with different computational protocols. CuI@Mo_2CO_2 has U_L values comparable to or smaller in magnitude than those of representative MXene-based NO_3RR catalysts reported so far. RuII@W_2CO_2 (−0.45 V) is also competitive with, or better than, most of these reported systems.

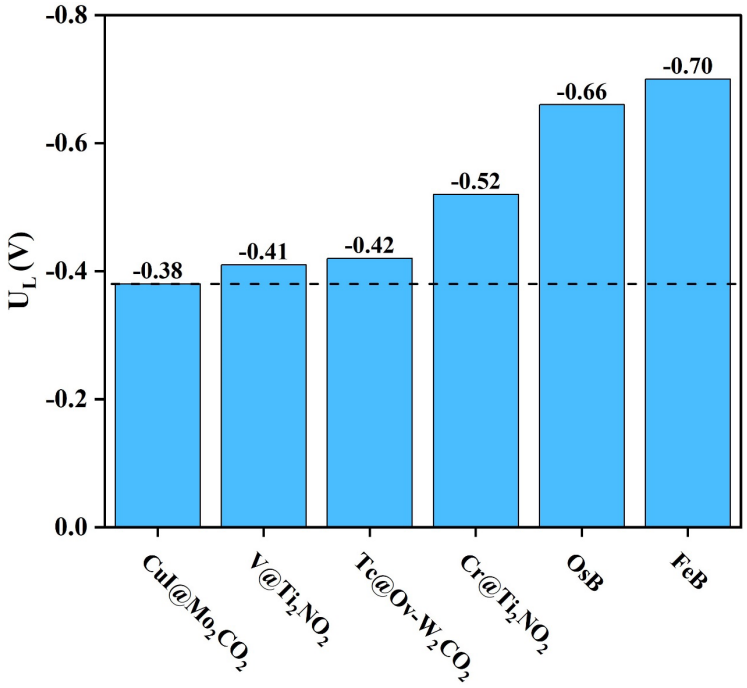


Figure 8. U_L of CuI@Mo_2CO_2 and other MXene catalysts.

3.4. Origin of the theoretically predicted catalytic activity of CuI@Mo_2CO_2 and RuII@W_2CO_2

To further elucidate the origin of the theoretically predicted catalytic activity of CuI@Mo_2CO_2 and RuII@W_2CO_2, we first investigated their electronic structures and charge transfer behaviors through charge density difference analysis and projected density of states (PDOS) calculations. As shown in Figure 9, NO_3^- adopts a bidentate chelating coordination configuration on both CuI@Mo_2CO_2 and RuII@W_2CO_2 surfaces through two oxygen atoms, forming two stable TM–O bonds. The Cu–O bond lengths are 2.041/2.049 Å, while the Ru–O bond lengths are 2.038/1.971 Å, indicating that both catalysts can achieve geometrically stable anchoring of the reaction substrate. Importantly, the TM–O bond length is not merely a geometric parameter but reflects the degree of orbital hybridization between the TM d states and the O 2p states of the adsorbed *NO_3. A shorter TM–O bond corresponds to stronger d–p hybridization and more pronounced charge transfer from the TM center to the adsorbed intermediate, which fills the antibonding orbitals of NO_3^-, weakens the intramolecular N–O bonds, and strengthens the TM–O interaction, thereby making the adsorption free energy more negative. This electronic effect can also be qualitatively understood in light of the general BEP principle, in which adsorption strength and the barrier of the subsequent hydrogenation step tend to scale with each other. Accordingly, a moderate TM–O bond length and the associated degree of charge transfer are expected to place the system near the Sabatier optimum, where the hydrogenation barrier is minimized. Our calculated structural and electronic parameters support this interpretation. The geometric anchoring brings the TM centers and adsorbed *NO_3 into strong electronic contact. This contact weakens the intramolecular N–O bonds. In free HNO_3, the N–O bond length is 1.21 Å. In adsorbed *NO_3 the bonds stretch to 1.301/1.307 Å on CuI@Mo_2CO_2 and 1.313/1.312 Å on RuII@W_2CO_2. This elongation shows directly that the N–O bonds are weakened and activated. Charge density difference maps (Figure 9) and Bader charge analysis show electron redistribution at the interface. Electrons move from the TM atoms to *NO_3. The transferred charge is

0.625 e^- for CuI@Mo_2CO_2 and 0.673 e^- for RuII@W_2CO_2. This electron donation fills the antibonding orbitals of NO_3^-. It is the main reason for N–O bond elongation and efficient nitrate activation.

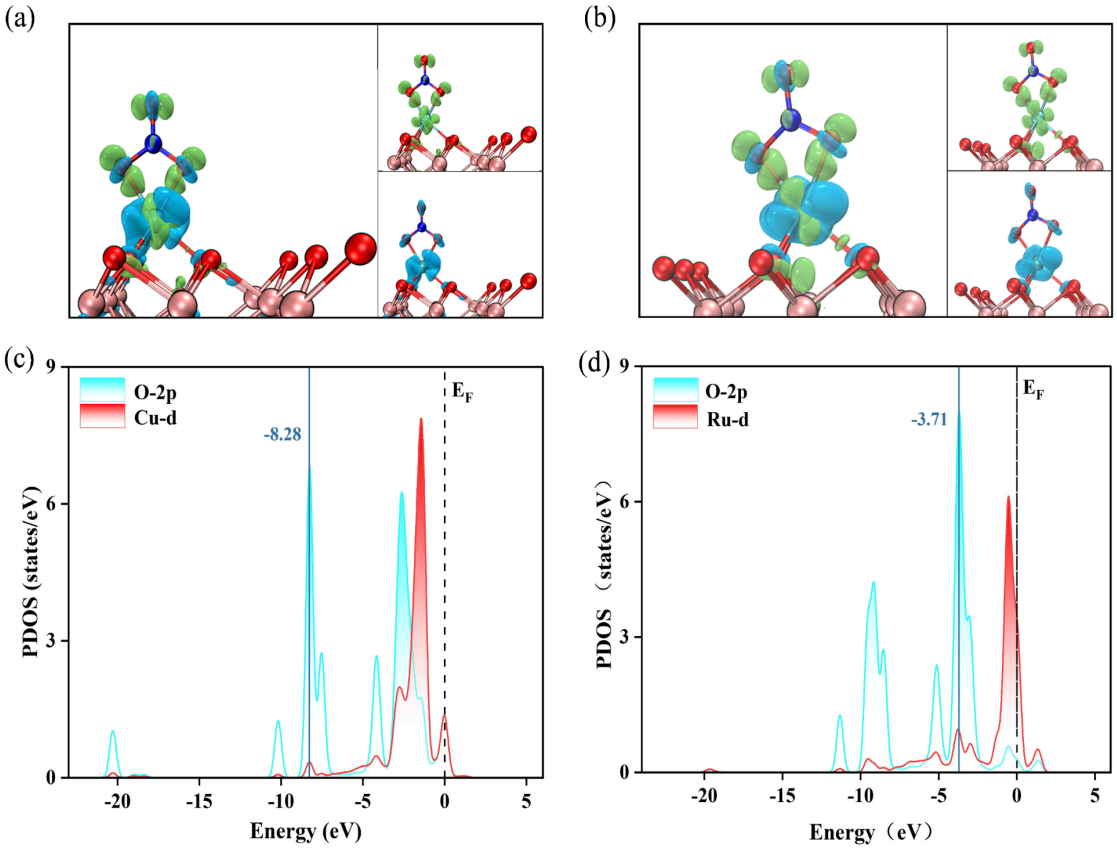


Figure 9. Charge density difference for NO_3^- adsorption on **(a)** CuI@Mo_2CO_2 and **(b)** RuII@W_2CO_2. Green isosurfaces: electron accumulation. Blue isosurfaces: electron depletion. PDOS of adsorbed NO_3^- on **(c)** CuI@Mo_2CO_2 and **(d)** RuII@W_2CO_2.

We then calculated PDOS with the Fermi level as reference to compare electronic conductivity and orbital interactions in the two systems (Figure 9c,d). Both systems show non-zero density of states near the Fermi level. Their band gaps are close to zero. This points to intrinsic metallic behavior. Such behavior provides a favorable electronic basis for fast interfacial electron transfer during electrocatalysis. For CuI@Mo_2CO_2, O p states lie mainly between −10 and 0 eV. Prominent peaks appear near −8.3, −4.2, and −2.6 eV. Cu d states are concentrated between −5 and 0 eV, with the main peak near −1.4 eV. The p and d states overlap at −4.2 and −2.7 eV and near the Fermi level. This overlap indicates strong p-d hybridization. For RuII@W_2CO_2, the main O p peak is around −3.7 eV. The dominant Ru d peak is at −0.53 eV, closer to the Fermi level. Hybridization in this system appears mainly around −5.2, −3.7, and −0.5 eV. Notably, RuII@W_2CO_2 exhibits a higher d-state density of states at the Fermi level, which endows the catalyst with enhanced electronic conductivity and more efficient interfacial charge transfer capability. In contrast, CuI@Mo_2CO_2 demonstrates a more balanced p–d orbital coupling feature, which is beneficial for preventing excessively strong intermediate adsorption and maintaining moderate adsorption strengths as well as favorable reaction selectivity. The distinct electronic structures of these two catalysts collectively underpin the electronic origin of their outstanding catalytic performance.

Building on this general bond-length–activity relationship, these electronic-structure results also account for the PDS divergence: *NO_3 → *NO_3H on CuI@Mo_2CO_2 *versus* *NO → *NHO on

RuII@W_2CO_2. On CuI@Mo_2CO_2, the d^{10} Cu center interacts only moderately with the bidentate *NO_3 group. This Cu–O covalency stabilizes *NO_3 without stretching its N–O bonds too far. The first protonation is therefore the hardest elementary step. In contrast, on RuII@W_2CO_2, the d^6 Ru site together with the more covalent W_2CO_2 substrate promotes stronger interfacial charge redistribution and a higher d-state density near the Fermi level (Figure 9d), which facilitates the early hydrogenation/dehydration steps and shifts the energetic bottleneck to *NO → *NHO; consistently, the stronger Ru–O bonds and the more pronounced N–O elongation indicate that *NO_3 is more strongly stabilized on RuII@W_2CO_2 and thus requires a higher barrier for subsequent N–H formation. In other words, the PDS divergence originates from the interplay between the intrinsic d-electron configuration/electronegativity of the single metal (Cu *vs* Ru) and the substrate-dependent charge-transfer capability (Mo_2CO_2 *vs* W_2CO_2), which together shift the Sabatier optimum along the reaction coordinate. It is worth emphasizing that stronger binding does not translate into higher activity: RuII@W_2CO_2 binds *NO_3 more strongly than CuI@Mo_2CO_2, but this over-stabilization raises the barrier of the subsequent *NO → *NHO step (0.45 eV *vs* 0.38 eV for the *NO_3 → *NO_3H step on CuI@Mo_2CO_2), placing RuII@W_2CO_2 on the strong-binding side of the Sabatier optimum and giving a more negative limiting potential. This is fully consistent with the bond-length–activity picture outlined above: the shorter Ru–O bonds on RuII@W_2CO_2 correspond to stronger d–p hybridization and stronger binding, which places this system on the strong-binding side of the Sabatier optimum, whereas the moderate Cu–O covalency on CuI@Mo_2CO_2 places it closer to the optimum and thus yields a lower hydrogenation barrier (0.38 eV *vs* 0.45 eV).

However, NO_3RR is a complex reaction network involving multiple PCET steps, and the structure–activity relationship governing catalytic performance is difficult to fully elucidate solely through qualitative electronic structure analysis. To complement the DFT analysis, ML was used to explore associations between physicochemical descriptors and the U_L among the 16 screened catalysts. Eleven initial descriptors were considered: nitrate adsorption free energy (ΔG_{*NO_3}), average TM–O bond length ($L_{TM\text{-}O}$), average TM–M bond length ($L_{TM\text{-}M}$), transition-metal atomic number (Num), first ionization energy (M_{ion}), second ionization energy ($M_{ion\text{-}2}$), electronegativity (χ_p), valence electron number (M_{val}), relative atomic mass (Mass), atomic radius (R), and electron affinity (E_{aff}). Their values are provided in Table S12. Given the small sample size, the ML analysis is intended as an exploratory examination of descriptor–activity associations rather than an independent determination of catalytic mechanisms.

Pearson correlation coefficients were calculated to examine pairwise linear associations between the 11 initial descriptors and U_L (Figure 10a and Table S13). The absolute correlation coefficients of ΔG_{*NO_3} and $L_{TM\text{-}M}$ with U_L were 0.37 and 0.45, respectively. Linear association in this dataset is therefore limited. We used 0.3 only as a heuristic reference for judging Pearson correlation coefficients. It is not a strict statistical cutoff. In this analysis, values above 0.3 were treated as relatively stronger pairwise linear associations. Values below 0.3 were treated as weaker. The descriptor correlation matrix showed a strong correlation between Mass and Num (r = 1.00; Figure 10b), and Mass was excluded to reduce redundancy. The other 10 descriptors were kept for regression modeling. Removing the redundant descriptor still leaves the sample-to-feature ratio limited. Weak pairwise correlations alone do not show nonlinear interactions.

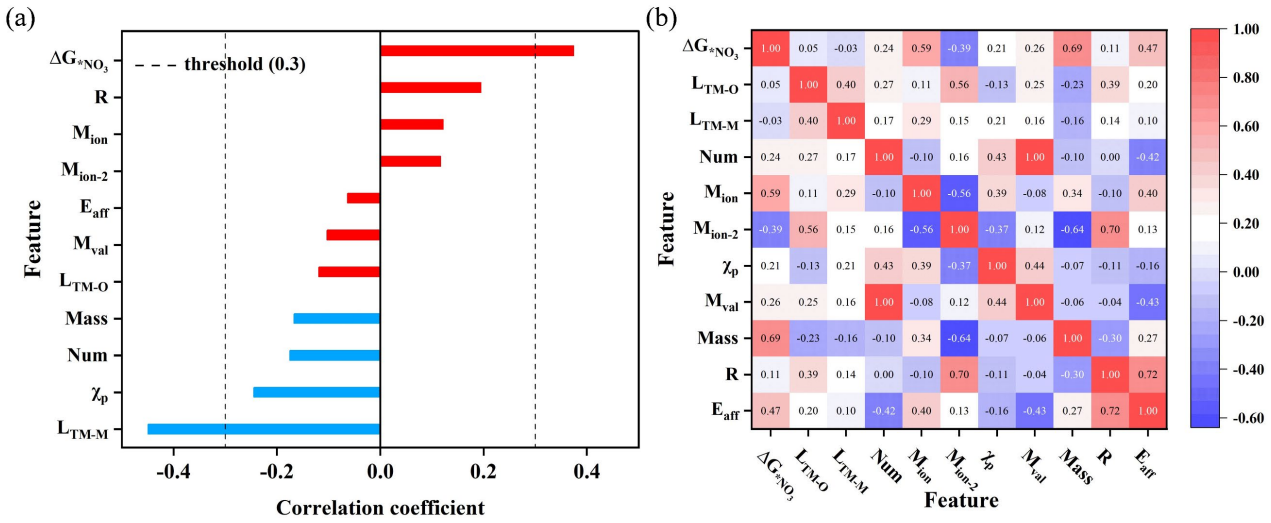


Figure 10. Correlation analysis of the 11 initial descriptors. **(a)** Pearson correlation coefficients between the 11 initial descriptors and the U_L; **(b)** Heatmap showing pairwise correlation coefficients among the 11 initial descriptors. The dashed line indicates the heuristic threshold of 0.3 used for interpreting correlation strength.

Four regression models, gradient boosting regression (GBR), random forest (RF), linear regression (LR), and ridge regression (RR), were evaluated. Training-set fitting and cross-validated performance are reported separately in Table 1 and Figure 11. GBR reached a training R^2 of 0.986, with MAE = 0.034 V and RMSE = 0.037 V (Figure 11a). RF, LR, and RR gave training R^2 values of 0.941, 0.799, and 0.582, respectively (Figure 11b–d). These numbers describe fits to the available data. They do not show how well the models predict unseen catalysts.

The regression set has only 16 screened systems. We started with 11 descriptors. Mass was removed because it correlated perfectly with Num (r = 1.00). Ten descriptors remained, so the sample-to-feature ratio is 1.6. With so few samples per feature, each feature offers little independent information for estimating relationships between descriptors and activity. Overfitting and unstable feature attribution are therefore real risks. Sequential stability and selectivity screening also narrows the chemical space represented by the data. We therefore treat the ML results only as exploratory associations within this selected set. Cross-validation gives internal performance estimates. It cannot make up for the small sample size. Nor can it support reliable extrapolation beyond the sampled chemical space.

LOOCV and 5-fold CV were used to test model performance on samples excluded from training. In LOOCV, each of the 16 samples was held out once. Pooling the 16 held-out predictions gave the performance metrics. For 5-fold CV, we used five different random partitions. In each run, the 16 out-of-fold predictions were pooled to compute the metrics. The 5-fold results are reported as the mean ±f standard deviation across the five runs.

Table 1. Training fit and cross-validation results for four U_L regression models.

Models	Training R^2	Training MAE (V)	Training RMSE (V)	LOOCV R^2	5-fold CV R^2
GBR	0.986	0.034	0.037	0.883	0.815 ± 0.139
RF	0.941	0.074	0.076	0.847	0.764 ± 0.193
LR	0.799	0.095	0.141	0.736	0.682 ± 0.230
RR	0.582	0.157	0.203	0.531	0.492 ± 0.318

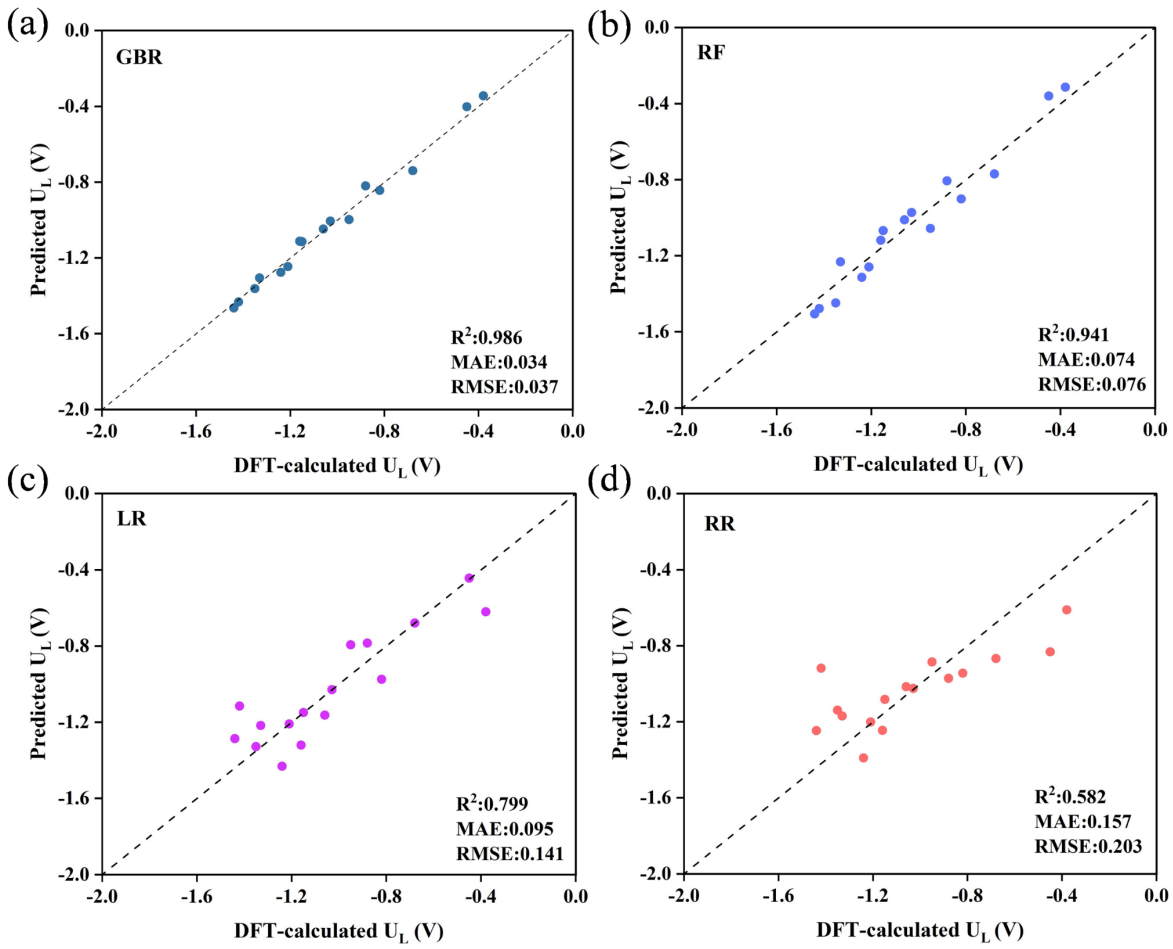


Figure 11. DFT-calculated U_L *versus* fitted U_L on the training set. Panels **(a)** GBR; **(b)** RF; **(c)** LR; **(d)** RR.

LOOCV gave R^2 values of 0.883 for GBR, 0.847 for RF, 0.736 for LR, and 0.531 for RR. In 5-fold CV, the values were 0.815 ± 0.139, 0.764 ± 0.193, 0.682 ± 0.230, and 0.492 ± 0.318 in the same order. The ranking did not change between the two schemes. GBR had the highest mean cross-validated R^2 and the smallest standard deviation, so we selected it for further interpretation. Its numerical lead over the other models does not show that the difference is statistically significant.

Cross-validation scores were lower than training scores. Fitting the training set alone therefore gives an overly optimistic picture of predictive performance. GBR and RF did better. This may mean that nonlinear models pick up more descriptor-activity associations in this dataset. Still, there are only 16 screened systems. The 5-fold results are sensitive to how the data are split. We treat these findings as internal validation only. They do not prove reliable generalization to unseen catalysts. RR performed poorly here, but this result is limited to the present dataset and model setup. It does not mean that linear models are inherently unsuitable.

Figure 12 shows the feature importance for each model. Within the fitted GBR model, $L_{TM\text{-}O}$, ΔG_{*NO_3} and χ_p receive the highest importance scores and dominate the model-derived importance ranking for this dataset; because this ranking is obtained from a 16-sample, 10-feature model, it is not converted into a percentage contribution and should not be interpreted as a stable or universal attribution. These scores characterize the fitted models and should not be interpreted as physical percentages of catalytic activity.

To further interpret the predictions, SHAP analysis was performed on the final GBR model fitted to all 16 systems (Figure 13a,b). The bee swarm plots and dependence plots for the RF and LR models are provided in Figures S15 and S16, respectively. The RR model is included in Figure 12 as a linear baseline for comparison of model-derived feature importance, but is not further interpreted via SHAP analysis. Its cross-validated performance is substantially lower and less stable ($R^2 = 0.492 \pm 0.318$), and it captures the descriptor-activity relationship less well than the nonlinear models in this dataset. For the fitted GBR model on the 16 systems, the SHAP summary plot ranks $L_{TM\text{-}O}$, ΔG_{*NO_3}, and χ_p as the three most influential descriptors by mean absolute SHAP value. This ranking matches the earlier importance analysis, but it should not be extended beyond the sampled chemical space. The remaining descriptors carry smaller SHAP contributions here. This agreement shows that these three descriptors are relevant to the fitted model. It does not prove they are causally significant.

The dependence plot shows a nonmonotonic SHAP contribution of $L_{TM\text{-}O}$. Data points with intermediate standardized bond lengths generally have negative contributions, whereas positive contributions occur at both smaller and larger bond lengths. Because the model predicts U_L directly, a positive SHAP value shifts the prediction toward more positive potentials relative to the model baseline. This pattern reflects descriptor attribution within the fitted model rather than the isolated causal effect of changing the bond length. The sampling is sparse, particularly at the extremes. A robust functional relationship or an optimal bond-length interval therefore cannot be identified.

We colored the dependence plot by ΔG_{*NO_3} to look for interaction patterns. Across the sampled range, no clear or consistent color separation appeared. This suggests nonlinear descriptor-prediction associations. It does not establish a definitive synergistic effect. With such a small dataset, we treat these findings as exploratory. Further calculations are needed to validate them.

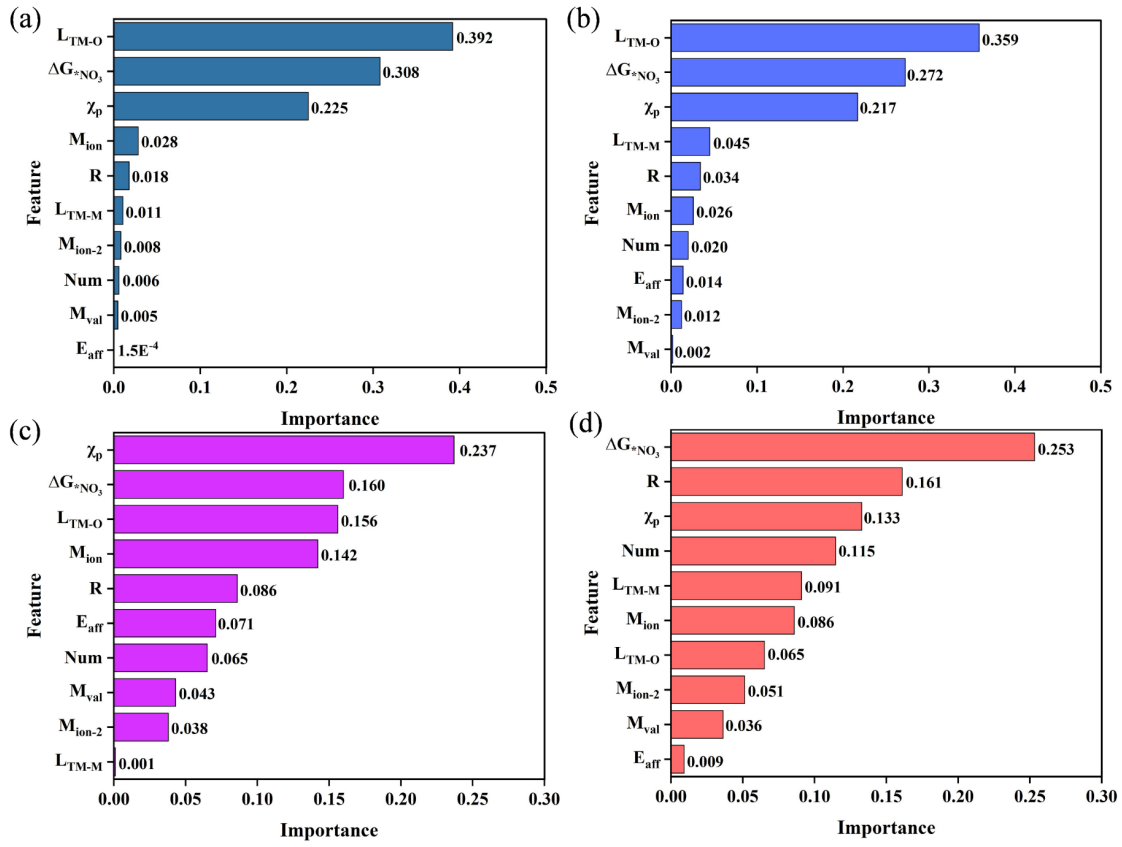


Figure 12. Feature importance distribution for the **(a)** GBR; **(b)** RF; **(c)** LR; **(d)** RR models.

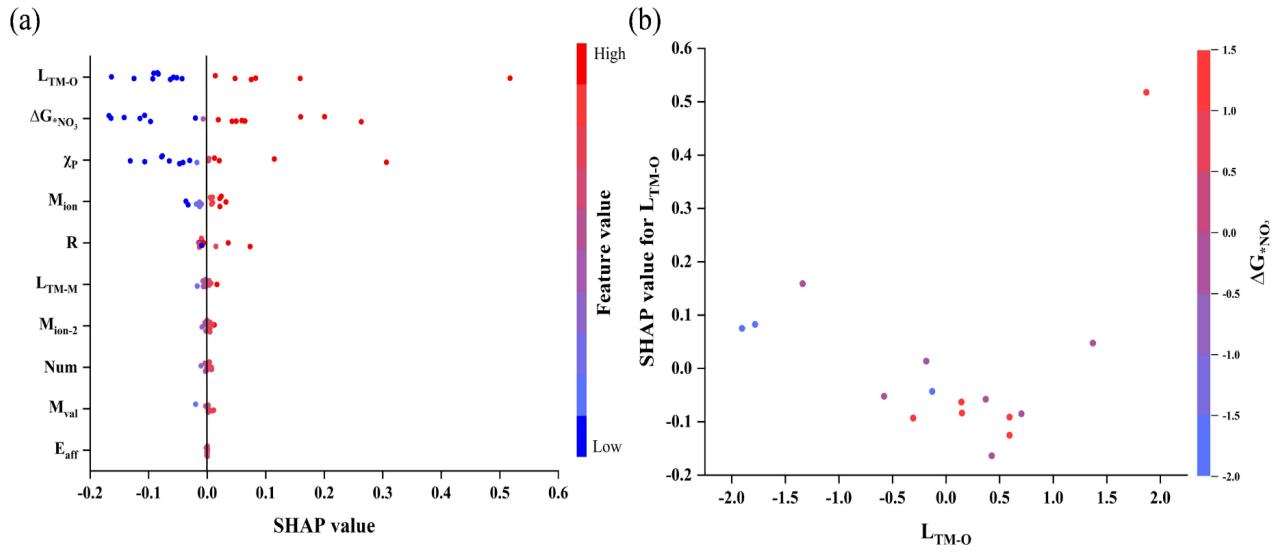


Figure 13. SHAP analysis of the final GBR model fitted to all 16 candidate systems. **(a)** SHAP summary plot, with colors indicating the corresponding feature values; **(b)** SHAP dependence plot of the TM–O bond length, colored by the nitrate adsorption free energy.

4. Conclusion

In this study, a combined strategy of DFT calculations and ML was employed to systematically investigate the catalytic performance of TM@M_2CO_2 systems, consisting of Cr_2CO_2, Mo_2CO_2, and W_2CO_2 substrates decorated with 3d–5d TM atoms, for electrocatalytic NO_3RR.

Through a stepwise screening process based on stability (formation energy and dissolution potential) and selectivity ($\Delta G_{*NO_3} < \Delta G_{*H}$), we progressively narrowed down the initial 150 systems to 16 viable candidates, among which two were identified as the most promising. Limiting potential calculations identify CuI@Mo_2CO_2 and RuII@W_2CO_2 as the most promising theoretical candidates among the investigated systems, with U_L values of −0.38 V and −0.45 V, respectively. Reaction pathway analysis and CI-NEB transition-state searches confirm that the PDSs of NO_3RR on both catalysts possess reasonable thermodynamic and kinetic barriers. The Volmer-Tafel barriers for HER are much higher than the NO_3RR PDS barriers on the same catalysts. HER is therefore kinetically less favorable than NO_3RR. Electronic structure analysis shows that NO_3^- binds to both surfaces through bidentate chelating coordination. Considerable charge moves from the TM centers to the adsorbed nitrate. The N–O bonds are strongly stretched. This stretching confirms that nitrate is effectively activated.

GBR gave the best internal cross-validation R^2 among the four regression models. LOOCV gave 0.883 and 5-fold CV gave 0.815 ± 0.139. Both are internal consistency scores on a 16-sample dataset. They do not show external predictive capability. SHAP analysis of the final GBR model picked out geometric and adsorption descriptors. It also pointed to a nonlinear link between the TM–O bond length and its contribution to the predicted limiting potential. For this dataset, these observations are exploratory hypotheses. They do not establish universal descriptors or a causal synergistic mechanism.

Overall, the DFT calculations identify TM@M_2CO_2 catalysts that look promising in theory. They also give insight into reaction energetics and electronic structure. ML adds a complementary exploratory analysis of descriptors. The dataset is small and pre-screened, so model comparisons, feature attribution, and extrapolation to unseen catalysts are all limited. A larger and more diverse dataset with independent

validation is needed to establish reliable predictive capability. Explicit kinetic verification covered only the two most promising catalysts. A broader kinetic assessment is still needed. On this basis, CuI@Mo_2CO_2 and RuII@W_2CO_2 are proposed as promising candidates for future experimental synthesis and electrochemical validation. Their predicted performance should be treated as theoretical at this stage.

Data availability statement

The authors confirm that the supplementary data is available within this article. This supporting material provides supplementary data and detailed characterization results that support the main findings of this work. It includes the free energy diagrams of the optimal NO_3RR pathways on 16 TM@M_2CO_2 catalysts, formation energies and dissolution potentials of anchored metals, adsorption free energies of NO_3^- and H, Gibbs free energy changes of competing pathways and elementary steps, SHAP analysis, selected descriptors and correlation analysis (PDF).

Declaration of generative AI and AI-assisted technologies

The authors did not use generative AI or AI-assisted technologies in the writing of this manuscript. The author takes full responsibility for the content of the manuscript.

Acknowledgments

Funding: this work was supported by the Advanced Materials-National Science and Technology Major Project (2026ZD0623600), Major Scientific and Technological Innovation Projects in Shandong Province (No. 2025ZLGX07), National Natural Science Foundation of China (U23B2087), and Shandong Provincial Natural Science Foundation (ZR2026MS0501, ZR2022MB094).

Authors' contribution

Conceptualization, J.X. and L.Z.; methodology, Y.Q.; software, L.Z.; validation, W.H., J.Z. and Y.L.; formal analysis, X.W.; investigation, J.X. and Y.Q.; resources, G.Z. and L.Z.; data curation, J.F., W.A., and Z.Z.; writing—original draft preparation, J.X. and Y.Q.; writing—review and editing, J. X. and L.Z.; visualization, X.L.; supervision, Y.L. and L.Z.; project administration, L.Z.; funding acquisition, G.Z. and L.Z. All authors have read and agreed to the published version of the manuscript.

Conflicts of interest

The authors declare no competing interests.

References

[1] Zhang Z, Zhang N, Zhang J, Deng B, Cao Z, *et al*. Critical review in electrocatalytic nitrate reduction to ammonia towards a sustainable nitrogen utilization. *Chem. Eng. J.* 2024, 483:148952.

[2] Hoang Truong N, Kim J, Lim J, Shin H. Electrochemical reduction of nitrate to ammonia: recent progress and future directions. *Chem. Eng. J.* 2024, 495:153108.

[3] Halder D, Sen S, Roy S. Recent advances in mechanistic studies and catalyst development for electrochemical nitrate reduction to ammonia. *Commun. Chem.* 2025, 9:58.

[4] Cui Z, Wang H, Li C, Peng W, Liu J. Electrochemical nitrate reduction reaction to ammonia at industrial-level current densities. *Adv. Sci.* 2026, 13(11):e23422.
[5] Bai J, Dong Z, Jiang X, Zhou Q, Zhao J, *et al.* Advancing nitrate-to-ammonia electrocatalysis: strategies in catalyst design, electrolyte engineering, and performance evaluation. *Adv. Sci.* 2025, 12(34):e08614.
[6] Cao Y, Yuan S, Meng L, Wang Y, Hai Y, *et al.* Recent advances in electrocatalytic nitrate reduction to ammonia: mechanism insight and catalyst design. *ACS Sustain. Chem. Eng.* 2023, 11(21):7965–7985.
[7] Liao G, Smith R, Guo H, Qi X. Review of carbon-based catalysts for electrochemical nitrate reduction and green ammonia synthesis. *Green Chem.* 2024, 26(24):11797–11831.
[8] Chen Q, Deng L, Zhang J, Zhang Y, Zhang L, *et al.* Carbon-based catalysts for electrochemical nitrate reduction to ammonia: design strategies and mechanistic insights. *Materials* 2025, 18(13):3019.
[9] Li H, Fu H, Zhang B, Sun C, Yin S. Recent advances in cu-based electrocatalysts for nitrate reduction to ammonia: from catalyst design to practical applications. *Phys. Chem. Chem. Phys.* 2026, 28(10):6148–6170.
[10] Subhadarshini S, Pumera M. Single atom catalyst for nitrate-to-ammonia electrochemistry. *Small* 2025, 21(28):2403515.
[11] Yang Y, Zhu J, Li W, Zhou M, Ye J, *et al*. Recent advances in single-atom catalysts for electrochemical nitrate reduction to ammonia. *J. Environ. Chem. Eng.* 2025, 13(1):115144.
[12] Yin S, Wang Y. Single-atom catalysts for electrochemical nitrate reduction to ammonia: rational design, mechanistic insights, and system perspectives. *Catalysts* 2025, 15(11):1084.
[13] Lv K, Wan H, Qi C, Wang W, Liu X, *et al.* Integrating AI and material science: MXene synthesis, preparation, and applications. *AI Mater.* 2025, 1(1):0004.
[14] Zeng X, Jin C, Zhang Z, Liu J, Zhao H. Construction of a 2D/2D MXene/TiO_2-MoS_2 heterostructure for highly efficient oxygen evolution reaction. *J. China Univ. Pet.* 2025, 49(5):220–226.
[15] Wang W, Li X, Deng Y, Jiang J, Ma H, *et al*. Advances in MXene-based single-atom catalysts for electrocatalytic applications. *Coord. Chem. Rev.* 2025, 529:216462.
[16] Yan X, Wang Y, Cai Y, Sharif H, Hou L, *et al.* MXene-based single-atom catalysts: synergistic interfaces and rational design for CO_2 electrocatalytic reduction. *Nano Res.* 2025, 18:94907748.
[17] Cui Z, Li C, Peng W, Liu J. Emerging MXene-based electrocatalysts for efficient nitrate reduction to ammonia: recent advance, challenges, and prospects. *Energy Mater*. 2024, 4(5):400057.
[18] Jan U, Mariappan K, Sakthinathan S, Chiu T, Tsai Y, *et al.* MXene-based catalysts for electrochemical nitrate and nitrogen reduction: a review toward sustainable nitrogenous fuels. *Sustain. Mater. Technol.* 2026, 47:e01892.
[19] Kui B, Zhao S, Hu Y, Zheng K, Yao Y, *et al.* Strongly coupled Ag/Cu with MXene for efficient tandem nitrate reduction reaction and zinc–nitrate batteries. *Catal. Sci. Technol.* 2025, 15(5):1617–1626.
[20] Phu T, Pham T, Nguyen A, Tran T, Le N, *et al*. Heterogeneous 2D/2D MnO_2/MXene catalyst for nitrate-to-ammonia electrochemical reduction and Zn-nitrate battery behavior. *iScience* 2025, 28(6):112729.
[21] Sharif H, Huang J, Mahmood A, Gao X, Cai Y, *et al*. Optimized electron transfer in Ru/Cu@MXene electrocatalysts for ultra-selective and high-yield electrochemical NH_3 synthesis. *Nano Mater. Sci.* 2025, in press.

[22] Luo S, Ma N, Zhao J, Wang Y, Zhang Y, *et al*. Theoretical regulating the M-site composition of Janus MXenes enables the tailoring design for highly active bifunctional ORR/OER catalysts. *J. Mater. Sci. Technol.* 2024, 199: 145–155.
[23] Nittoor-Veedu R, Ju X, Langer M, Gao W, Otyepka M, *et al.* Periodic table exploration of MXenes for efficient electrochemical nitrate reduction to ammonia. *Small* 2025, 21:2410105.
[24] Wang M, Hu T, Wang C, Du F, Yang H, *et al*. Screening MXene-based single-atom catalysts for selective nitrate-to-ammonia electroreduction. *Sci. China Mater.* 2023, 66:2750–2758.
[25] Lu Z, Liu J, Li H, Li R, Zhang X, *et al*. Leveraging machine learning to expedite screening of single-atom catalysts in electrochemical nitrate reduction to ammonia. *J. Alloys Compd.* 2025, 1010:177180.
[26] Li Y, Wang Y. Machine learning-powered high-throughput designing and screening of electrocatalysts for nitrate reduction to ammonia. *Chem. Eng. J.* 2026, 534:175353.
[27] Samreen A, Azim M, Chen F. Reinforcement learning world models for catalyst surface reconstruction: state-of-the-art review. *AI Mater.* 2025, 2:0011.
[28] Qi C, Wang W, Lv K, Li D, Liu Y, *et al.* Catalytic applications of 2D materials aided by machine learning. *AI Mater.* 2025, 1(2):0014.
[29] Zhu R, Wang H, Tang K, Yang X, Zhao X, *et al*. Single-atom collaboration with cluster for accelerated nitrate electroreduction: synergy revelation via machine learning and DFT calculations. *J. Energy Chem.* 2026, 112: 842–851.
[30] Wang S, Liu C, Hao W, Zhu X, Niu X, *et al*. Machine learning accelerates the design and discovery of single-atom catalysts for electrochemical reactions. *J. Energy Chem.* 2026, 115: 347–371.
[31] Hu Z, Wang Z, Peng Y, Gao Z, Jin C, *et al*. Machine learning-guided design of energy-related catalysts from nanoparticles to single-atom sites. *Commun. Chem*. 2026, 9:128.
[32] Mu J, Gao X, Yu T, Zhao L, Luo W, *et al*. Ambient electrochemical ammonia synthesis: from theoretical guidance to catalyst design. *Adv. Sci*. 2024, 11:2308979.
[33] Liu J, Richards D, Singh N, Goldsmith B. Activity and selectivity trends in electrocatalytic nitrate reduction on transition metals. *ACS Catal.* 2019, 9(8):7052–7064.
[34] Zheng S, Li S, Mei Z, Hu Z, Chu M, *et al.* Electrochemical nitrogen reduction reaction performance of single-boron catalysts tuned by MXene substrates. *J. Phys. Chem. Lett.* 2019, 10(2):6984–6989.
[35] Li H, Wei S, Wang H, Cai Q, Zhao J. Enhanced catalytic activity of MXene for nitrogen electoreduction reaction by carbon doping. *J. Colloid Interface Sci.* 2021, 588:1–8.
[36] Shen Z, Fan X, Ma S, An Y, Yang D, *et al.* 3d transitional-metal single atom catalysis toward hydrogen evolution reaction on MXenes supports. *Int. J. Hydrogen Energy* 2020, 45:14396–14406.
[37] Lin G, Guo T, Lin W, Fan H, Guo L, *et al*. Machine learning accelerated screening advanced single-atom anchored MXenes electrocatalyst for nitrogen fixation. *ACS Catal.* 2025, 15:13534–13548.
[38] Delley B. DMol^3 DFT studies: from molecules and molecular environments to surfaces and solids. *Comput. Mater. Sci.* 2000, 17:122–126.
[39] Jing T, Liang D, Deng M, Cai S, Qi X. Density functional theory studies of heteroatom-doped graphene-like GaN monolayers as electrocatalysts for oxygen evolution and reduction. *ACS Appl. Nano Mater.* 2021, 4:7125–7133.
[40] Perdew J, Burke K, Ernzerhof M. Generalized gradient approximation made simple. *Phys. Rev. Lett.* 1996, 77:3865–3868.

[41] Zhao L, Han W, Yan G, Peng Z, Ding T, *et al.* CoCu dual-atom driven high-efficiency electrocatalysis of methane to methanol. *J. China Univ. Pet.* 2025, 49:227–235.
[42] Grimme S, Antony J, Ehrlich S, Krieg H. A consistent and accurate ab initio parametrization of density functional dispersion correction (DFT-D) for the 94 elements H-Pu. *J. Chem. Phys.* 2010, 132:154104.
[43] Qu Y, Ding J, Chen H, Peng J. Effect of noble metal atoms on adsorption and electronic properties of graphene toward toxic gas. *Comput. Theor. Chem.* 2021, 1196:113115.
[44] Xiao B, Yang L, Liu H, Jiang X, Aleksandr B, *et al.* Designing fluorographene with FeN_4 and CoN_4 moieties for oxygen electrode reaction: a density functional theory study. *Appl. Surf. Sci.* 2021, 537:147846.
[45] Jacob C, Reiher M. Spin in density-functional theory. *Int. J. Quantum Chem.* 2012, 112:3661–3684.
[46] Mathew K, Kolluru V, Mula S, Steinmann S, Hennig R. Implicit self-consistent electrolyte model in plane-wave density-functional theory. *J. Chem. Phys.* 2019, 151:234101.
[47] Todorova T, Delley B. Wetting of paracetamol surfaces studied by $DMol^3$-COSMO calculations. *Mol. Simul.* 2008, 34:1013–1017.
[48] Rumble JR. *CRC Handbook of Chemistry and Physics*, 98th ed. Boca Raton: CRC Press, 2017.
[49] Wang S, Gao H, Li L, Hui K, Dinh D, *et al.* High-throughput identification of highly active and selective single-atom catalysts for electrochemical ammonia synthesis through nitrate reduction. *Nano Energy* 2022, 100:107517.
[50] Niu H, Zhang Z, Wang X, Wan X, Shao C, *et al.* Theoretical insights into the mechanism of selective nitrate-to-ammonia electroreduction on single-atom catalysts. *Adv. Funct. Mater.* 2021, 31:2008533.
[51] Nørskov J, Rossmeisl J, Logadottir A, Lindqvist L, Kitchin J, *et al*. Origin of the overpotential for oxygen reduction at a fuel-cell cathode. *J. Phys. Chem. B* 2004, 108:17886–17892.
[52] Badawi K, Sharazly B, Negm O, Khan R, Carter W. Is cadmium genotoxicity due to the induction of redox stress and inflammation? A systematic review. *Antioxidants* 2024, 13(8):932.
[53] Qian J, Bai S, Geng M, Zhang D, Xiang G, *et al*. Construction of low-toxicity cadmium sulfide/nitrogen-doped muti-walled carbon nanotubes for peroxymonosulfate activation: the crucial role of electron transfer. *Environ. Res.* 2025, 266:120582.
[54] Wang L, Dou Y, Gan R, Zhao Q, Ma Q, *et al*. The single atom anchoring strategy: rational design of MXene-based single-atom catalysts for electrocatalysis. *Small* 2025, 21(11):2410772.
[55] Chen G, Yuan Y, Jiang H, Ren S, Ding L, *et al.* Electrochemical reduction of nitrate to ammonia via direct eight-electron transfer using a copper–molecular solid catalyst. *Nat. Energy* 2020, 5:605–613.
[56] Laursen A, Man I, Trinhammer O, Rossmeisl J, Dahl S. The sabatier principle illustrated by catalytic H_2O_2 decomposition on metal surfaces. *J. Chem. Educ.* 2011, 88(12):1711–1715.
[57] Pang Y, Ding Z, Ma A, Fan G, Xu H. Electroreduction of nitrate to ammonia on graphyne-based single-atom catalysts by combined density functional theory and machine learning study. *Sep. Purif. Technol.* 2025, 354:129422.
[58] Ai F, Wang J. Theoretical evaluation of electrochemical nitrate reduction reaction on graphdiyne-supported transition metal single-atom catalysts. *ACS Omega* 2022, 7:31309–31317.
[59] Ma C, Zhang H, Xia J, Zhu X, Qu K, *et al.* Screening of intermetallic compounds based on intermediate adsorption equilibrium for electrocatalytic nitrate reduction to ammonia. *J. Am. Chem. Soc.* 2024, 146:20069–20079.

[60] Ren Z, Shi K, Feng X. Elucidating the intrinsic activity and selectivity of Cu for nitrate electroreduction. *ACS Energy Lett.* 2023, 8:3658–3665.

[61] Jia K, Luo W, Wang W, Cheng Y. A study leveraging first-principles calculations and machine learning to investigate the electrocatalytic nitrate reduction performance of single-atom supported on defective MXene (M = Cr, Mo, and W). *Appl. Catal. A-Gen.* 2026, 709:120640.

[62] Cheng Y, Wang W, Shao C. Revealing the origin of activity and selectivity in nitrate to ammonia conversion on single transition metal atom catalysts supported by a Ti_2NO_2 monolayer. *Phys. Chem. Chem. Phys.* 2025, 27:4202–4210.

[63] Ho T, Nguyen Q, Le B, Kim S, Bui V. Unlocking electrocatalytic dynamics with anti-MXene borides monolayers for nitrate reduction. *Appl. Surf. Sci.* 2024, 674:160908.

[64] Hammer B, Hansen L, Nørskov J. Improved adsorption energetics within density-functional theory using revised Perdew–Burke–Ernzerhof functionals. *Phys. Rev. B* 1999, 59:7413–7421.

[65] Araujo R, Rodrigues G, Santos E, Pettersson L. Adsorption energies on transition metal surfaces: towards an accurate and balanced description. *Nat. Commun.* 2022, 13:6853.

[66] Zhang Q, Asthagiri A. Solvation effects on DFT predictions of ORR activity on metal surfaces. *Catal. Today* 2019, 323:35–43.